

## A Single-Dot Perovskite Spectrometer

*Linqi Guo, Haoxuan Sun\*, Min Wang, Meng Wang, Liangliang Min, Fengren Cao, Wei Tian, Liang Li\**

School of Physical Science and Technology, Jiangsu Key Laboratory of Thin Films, Center for Energy Conversion Materials & Physics (CECMP), Soochow University, Suzhou 215006, P. R. China

Email: [lli@suda.edu.cn](mailto:lli@suda.edu.cn); [hxsun@suda.edu.cn](mailto:hxsun@suda.edu.cn)

**Keywords:** perovskite, ion migration, spectrometer, hyper-spectrum

There are significant applications for miniature on-chip spectrometers in many fields. However, at present, on-chip spectrometers have to utilize an integrated strategy to achieve spectral analysis, which undoubtedly squanders the photosensitive area and adds pressure to the miniaturization of the spectrometer. Here, we demonstrate a unique spectrometer design that adopts a single detection point with in situ modulation realized by the photo-gain control at various bias voltages. With micrometre-level footprints, this single-dot spectrometer processes a resolution of about 5 nm and a response time down to about 197  $\mu$ s. This is the first in situ perovskite modulation strategy that breaks the footprint-resolution restriction of spectrum analysis and demonstrates a new design direction for functional perovskite devices.

This article has been accepted for publication and undergone full peer review but has not been through the copyediting, typesetting, pagination and proofreading process, which may lead to differences between this version and the [Version of Record](#). Please cite this article as [doi: 10.1002/adma.202200221](https://doi.org/10.1002/adma.202200221).

This article is protected by copyright. All rights reserved.

## 1. Introduction

Spectrometers are indispensable in many scientific fields and industrial applications, such as in biological sciences,<sup>[1]</sup> astronomy,<sup>[2]</sup> materials science,<sup>[3]</sup> and alloy analysis.<sup>[4]</sup> With the development of micro/nano-optics and microelectronics, a miniature on-chip spectrometer with high spectral resolution is required.<sup>[5-14]</sup> As shown in **Figure 1a**, the most prominent strategies of spectrometers can be grouped into four categories:<sup>[15]</sup> (i) Dispersion elements are utilized to achieve the separation of spectral components,<sup>[16]</sup> (ii) filters that selectively transmit light of a specific wavelength are integrated with the detector, (iii) a Fourier transform system is utilized to analyse the spectrum,<sup>[17]</sup> and (iv) a newly emerged scheme that exploits computational techniques to reconstruct the incident spectrum from the pre-set spectrum detection information.<sup>[7-10]</sup> It is obvious that all devices that contain complex optical or mechanical components (e.g., the linear variable filter spectrometer, waveguide grating spectrometer and the Fabry-Pérot spectrometer) cannot be miniaturized adequately. Others usually deploy wavelength-selective components onto a horizontally distributed photodetector, which inevitably suffers from footprint-resolution restriction. Even the newly emerged device designs, namely, the charge collection narrowing (CCN)<sup>[18]</sup> spectrometer and reconstructive spectrometer,<sup>[7-9]</sup> which free the device from any optical/mechanical component, require multi-point integration, and the footprint-resolution limitations still exist.

Some studies have tried to construct vertically distributed integrated devices.<sup>[19-21]</sup> This may solve the dilemma, yet the spectral resolution is still limited by the number of integrated detection points. Thanks to the development of reconstruction algorithms, any excitation source that can tailor the device spectrum response is potentially practicable.<sup>[15]</sup> To prevent footprint-resolution limitations, in situ spectrum response modulation is an efficient design concept. By sacrificing the response speed, the spectral resolution can be theoretically unlimited, and the device footprint can reach the micron level (considering light diffraction, further improvement is unnecessary).

Recently, a single tunable black phosphorous (BP) spectrometer was proposed to solve resolution and footprint limitation.<sup>[6]</sup> This work provided a new idea for the miniaturization of spectrometers. However, the integration of this BP spectrometer would require the large-scale preparation of ultra-thin single crystals, and the use of the Stark effect to tune the photoelectric response would suffer from temperature limitations. Hybrid organic-inorganic perovskites, a well-studied semiconductor family, not only possess high carrier mobility and a suitable bandgap but also have adjustable components and energy band structures.<sup>[22]</sup> This makes them perfect materials for spectrum response modulation. Based on our previous work, the utilization of perovskite diodes has a response speed advantage.<sup>[8]</sup>

In this work, we propose a reconstructive single-dot spectrometer, which is enabled by photo-gain manipulation controlled by ion redistribution in the perovskite film under an

externally applied bias. As a single device, this spectrometer possesses a footprint of  $440 \times 440 \mu\text{m}^2$ , and the spectral resolution can reach up to about 5 nm. The response time can decrease to the microsecond level owing to the ultrafast optical response of perovskite. This manuscript is the first to propose a perovskite device based on in situ dynamic modulation, extending into a new field for perovskite functional devices and exerting a significant role in hyperspectral remote sensing and ultrahigh-resolution imaging.

## 2. Results and Discussion

### 2.1. The Design of Single-Dot Perovskite Spectrometer

The working mechanism of the single-dot perovskite spectrometer is derived from the reconstructive spectrometer, which is illustrated in Figure 1b. The detector is illuminated by an unknown incident light  $P(\lambda)$ , and a photocurrent measuring instrument records the current value  $I$  generated from the detector at different biases, followed by data analysis. A mapping relationship can be established between  $P$  and  $I$  via the photoresponsivity  $R$ , and finally,  $P(\lambda)$  can be reconstructed by solving a system of linear equations:

$$\int_{\lambda_1}^{\lambda_2} P(\lambda) R_i(\lambda) d\lambda = I_i \quad (i = 1, 2, 3, \dots, n)$$

Where  $\lambda_1$  and  $\lambda_2$  denote the start and cut off wavelengths, respectively (Please refer to the experimental section for detailed reconstruction process, Supporting Information).

Unlike other reconstructive spectrometers which integrate multiple detectors to realize the responsivity richness,<sup>[8,9,13]</sup> this single-dot spectrometer tunes the spectral responsivity of a single detector through controlling the ion migration in the active layer by external bias. It should be noted that light with different frequencies possesses different penetrating capabilities for perovskites. The applied bias, which is mainly concentrated in the depletion area, provides device photo-gain.<sup>[18,23]</sup> It is reasonable to suppose that ion migration, which is always considered a side effect with the use of perovskites, could be the approach to adjust the location of the depletion area and achieve photo-gain modulation.<sup>[24,25]</sup> As shown in Figure S1a, the electric field distribution of incident light with various energies is simulated by finite difference time domain (FDTD) solutions. It suggests that when a composite light is interacted with perovskite, the distribution of photogenerated carriers is asymmetric along the thickness. Most of the carriers are generated near the interface of perovskite/SnO<sub>2</sub>, and only the carriers excited by the photons with long wavelength can exist near the interface of perovskite/Spiro-OMeTAD. Meanwhile, according to previous research, it is easy to realize that the distribution of built-in electric field inside the perovskite absorber is also asymmetric along the direction of thickness.<sup>[24-26]</sup> Usually, due to the halogen loss during the annealing process, the perovskite is electron-rich. The PbX-rich surface will not only lead to bandgap narrowing but also create a n-type carrier status. When such n-type surface contact with Spiro-OMeTAD, it creates a stronger (compared with perovskite/SnO<sub>2</sub> interface) built-in electric field. It should be noted that even without the relative n-type surface, this conclusion

still stands since the perovskite is overall electron-rich. The stronger built-in electric field will lead to another fact that the external voltage mainly falls at the interface of perovskite/Spiro-OMeTAD. The photo-gain should mainly be provided at the same location. As we know that the photo-gain mainly originates from the unbalanced carriers. When the bias is applied, the ion migration will occur at the main junction area which is located at the perovskite/ Spiro-OMeTAD, and provides a large number of defects which acts as minority carrier traps and exacerbates the imbalance of carriers. When the bias increases, there is no doubt that such depletion region at the interface of perovskite/Spiro-OMeTAD should expand towards the side of perovskite/SnO<sub>2</sub>. However, the ion migration will retard this process because the additional electric field provided by the ion redistribution shields and consumes part of the external bias. That means, actually, the ion migration, the voltage drop and the photo-gain generation will appear at the same location. As shown in Figure S1b, when the bias increases, such area will shift towards the interface of perovskite/SnO<sub>2</sub>. The closer to the perovskite/SnO<sub>2</sub> interface, the higher photo-gain of short wavelength photon will be generated. Such phenomenon does not require special adjustment of perovskite and can be perceived in other literatures.<sup>[27,28]</sup> This makes the design of in-situ modulation even more feasible.

However, the redistribution of intrinsic perovskite ions induced by an external electric field usually leads to following problems:<sup>[29,30]</sup> (i) Irreversible long-range ion migration occurs. (ii) The migration of ions will cause irreversible collapse of the perovskite lattice and affect its

optical properties. Hence, we not only must suppress the redistribution of the intrinsic ions of the perovskite but also need to introduce external ions to alter the ion distribution state of the perovskite film in an external field. Many studies have reported that alkali metal ions (such as  $K^+$ ,  $Na^+$ , and  $Li^+$ ) can enter the perovskite lattice, therefore increasing the barrier energy for the migration of intrinsic halogen ions;<sup>[31,32]</sup> furthermore, ions with a small radius more easily alter the distribution state in an external electric field.<sup>[33,34]</sup> For this reason, LiCl is introduced as an additive to replace the migration of intrinsic halogen ions and act as a “regulator” for the alteration of the ion distribution state in perovskites.

## 2.2. The Ion Migration Manipulation with LiCl Additive

We verified the more severe ion redistribution in  $Cs_{0.05}MA_{0.15}FA_{0.8}PbI_{0.85}Br_{0.15}$  films<sup>[35]</sup> with LiCl doping through the measurement of the ion migration activation energy ( $E_a$ ) and ion conductivity ( $\sigma_{ion}$ ). **Figure 2a** shows the  $E_a$  of the different perovskite films (please refer to Figure S2 for the device structure, Supporting Information). The  $E_a$  in the control perovskite film is fitted to be 0.52 eV. However, the  $E_a$  is significantly decreased to 0.38 eV in the 5% LiCl-doped perovskite film, which indicates severe doping-induced ion migration. By applying a fixed current (0.5 nA) and recording the voltage value of the perovskite film, the conductivity of the film was obtained. Figure 2b shows the  $\sigma_{ion}$  of various perovskite samples. The control  $Cs_{0.05}MA_{0.15}FA_{0.8}PbI_{0.85}Br_{0.15}$  film exhibits a lower  $\sigma_{ion}$  of  $2.4 \times 10^{-11}$  S

$\text{cm}^{-1}$  compared to the film with 5% LiCl doping, which exhibits an  $\sigma_{\text{ion}}$  of  $6.1 \times 10^{-11} \text{ S cm}^{-1}$ . On the basis of the obtained  $E_a$  and  $\sigma_{\text{ion}}$  results, a conclusion can be drawn that the ions not only more easily migrate but also move faster in a LiCl-doped perovskite film.

Figure S3 (Supporting Information) exhibits the XRD patterns of LiCl-doped perovskite films monitored in the  $2\theta$  range of  $5-50^\circ$  as the lithium fraction was varied up to 15%. The XRD pattern shows an obvious diffraction peak located at  $14.13^\circ$ , which is indexed to the (110) plane of perovskite. As the doping concentration increases, the main diffraction peak located at  $14.13^\circ$  begins to shift towards a lower angle, which indicates that the lattice constant of perovskite with  $\text{Li}^+$  is larger. These XRD patterns confirm the interstitial occupancy of extrinsic  $\text{Li}^+$ , according to previous density functional theory (DFT) calculations.<sup>[33]</sup> In addition, no new peaks appear as the lithium fraction increases, indicating that the introduction of LiCl will change only the lattice constant of the perovskite but will not alter the lattice structure of the perovskite, and it will not generate a new phase. To investigate the evolution of the perovskite film under external bias, we imposed a bias (0.5 V) to a vertical device (Ag/Spiro-OMeTAD/perovskite/ $\text{SnO}_2$ /ITO, see Figure S4, Supporting Information) and characterized the properties of this perovskite film before (and after) bias was applied. For the control sample and the LiCl-doped sample, there is no change in the peak position of the perovskite before and after the external bias is applied, and no new diffraction peaks appear. These results indicate that the redistribution of the ions induced by the external electric field does not alter the principal perovskite lattice structure (see Figure



S5a and Figure S5b, Supporting Information). However, the directional drift of ions (halogen ions are enriched at the interface of perovskite/SnO<sub>2</sub>, where A-site cations are centralized at the interface of perovskite/Spiro-OMeTAD) should exist due to the low ion mobility activation energy of the LiCl-doped film. To prove this conjecture, glancing-angle ( $\omega$ ) XRD analysis was used to explore the longitudinal section of the perovskite film. As exhibited in Figure 2, both PbX (X = Cl<sup>-</sup>, Br<sup>-</sup>, I<sup>-</sup>) and perovskite XRD peaks of all films (with and without LiCl and with and without bias), from their bottom to surface, shift to lower angles because halide ions with small radii (Br<sup>-</sup>, Cl<sup>-</sup>) are easier to volatilize during the annealing process, leaving I<sup>-</sup>, which has a larger radius. In addition, without an external electric field, the (110) peak deviation of the LiCl-doped perovskite is more severe, which is due to the easier volatilization of additional Cl<sup>-</sup> ions with smaller radii. Furthermore, the content of PbI<sub>2</sub> on the surface is slightly reduced after an external bias is applied (0.5 V). The reason for this result is that the ions (MA<sup>+</sup>/FA<sup>+</sup>) driven by an external electric field migrate to the surface, which will react with the superfluous PbI<sub>2</sub> at the surface and regenerate the perovskite phase.

Photoluminescence (PL) spectra in **Figure 3a** show that the emission peaks of the control sample appear to obviously redshift as the bias increases, when the ITO side (back) of the device is exposed to the excitation light source. In contrast, as shown in Figure 3b, there is an obvious blueshift when the Spiro-OMeTAD side (front) becomes the incident surface. It should be noted that due to the annealing process, the perovskite film is not homogeneous. Usually, the surface shows a PbX-rich phase, while the bottom shows an AX (A = MA<sup>+</sup>, FA<sup>+</sup>)-

rich (compared with the original surface) phase.<sup>[25,26]</sup> When the perovskite becomes PbX-rich, it leads to bandgap narrowing, which can be rationalized by regarding the unsaturated chemical bonds of the surface Pb and I as shallow trap states.<sup>[36]</sup> During bias application, as we formerly proposed in XRD analysis, the A<sup>+</sup> ion migrating from the bottom will consume the original superfluous PbI<sub>2</sub> and even leave the bottom PbX-rich state. Eventually, the bottom and surface seem to switch with each other with an applied 0.5 V bias. Such intrinsic ion migration has side effects that greatly increase the defect level, which broadens the full width at half maximum (FWHM). As shown in Figure 3c and Figure 3d, when bias is applied to the LiCl-doped perovskite, only slight peak shifting is observed. It should be noted that the doped perovskite has a lower activation energy  $E_a$  and higher ion mobility. The only reasonable explanation is that the migration of the additional Li<sup>+</sup>/Cl<sup>-</sup> ion replaces the intrinsic ion migration of A<sup>+</sup> and X<sup>-</sup>, which does not cause lattice collapse (consistent with the former XRD analysis) and does not change the optical properties of the as-fabricated film (consistent with the later absorption and transmission analysis). The ion redistribution inside the LiCl-doped perovskite only shifts the position of the depletion layer, which modulates the wavelength-related photo-gain and suppresses the side effects of voltage modulation. In addition, since the difference between the surface and bottom is due to AX-component evaporation, perovskite with LiCl doping shows a longer peak distance, which is consistent with the XRD analysis.

UV-vis absorption and transmission spectra were also obtained in situ to confirm the previous conclusion. As shown in Figure S6a and Figure S6b (Supporting Information), at approximately 800 nm, as the external bias is increased, the transmittance values of the LiCl-doped sample and control sample both decrease, corresponding to an increase in the absorption value (see Figure S6c and Figure S6d, Supporting Information). The ion migration-induced shallow-level defects cause the film to undergo sub-band-gap absorption.<sup>[37]</sup> Apparently, the absolute value of the decrease in the transmission spectrum (as well as the increase in absorption value) of the perovskite film containing LiCl is smaller, which is due to the decrease in the migration of original ions.

To observe the ion redistribution in situ with the application of bias, time-of-flight secondary ion mass spectrometry (TOF-SIMS) was performed. As shown in Figure S7 (Supporting Information), for the perovskite films not exposed to an external electric field, the halogen ions are approximately evenly distributed throughout the film (see Figure S7a and Figure S7b, Supporting Information). However, after the application of an external bias of 0.5 V, the ion distributions of the control sample and LiCl-doped sample exhibit significant differences. It should be noted that the distribution of halogen ions can be regarded as a tracer that shows the concentrated area of bias voltage. The ion migration introduced by the electric field is against the bias voltage and the original built-in electric field, which means that the main area of ion redistribution corresponds to the main area with a voltage drop. From the above XRD and PL analysis, the perovskite is confirmed to be PbX-rich and an n-type

semiconductor.<sup>[26]</sup> Therefore, the main depletion layer should be primarily located at the Spiro-OMeTAD/perovskite interface. When a bias is applied, ion migration shall first occur at such a depletion layer since it is the main area with a voltage drop. The halide ion will be transported towards the ITO side, shifting the main area with a voltage drop along with it. When the system is balanced, the main ion redistribution area is formed. Such an area consumes most of the applied bias and provides the majority of photo-gain.<sup>[38]</sup> Figure S7c (Supporting Information) shows the main ion redistribution area at approximately 150-200 nm from the Spiro-OMeTAD side for the original perovskite. The main redistributed ions are  $I^-$  and  $Br^-$ . Compared with that, Figure S7d (Supporting Information) shows that the main redistributed ion becomes  $Cl^-$  for the doped perovskite, and the main redistributed area is located at the bottom of the film (ITO side). Additionally, since the  $Cl^-$  ion cannot shield all of the applied bias, an  $I^-$  and  $Br^-$  redistribution area still exists and is located at the Spiro-OMeTAD/perovskite interface where ion migration starts. The electrochemical impedance spectroscopy (EIS) results can also explain the phenomenon of ion aggregation at the interface between the perovskite and carrier transport layer (CTL). As exhibited in Figure S8 (Supporting Information), the transmission impedance ( $R_{ct}$ ) of the LiCl-doped and control samples improve. The increase in  $R_{ct}$  is ascribed to the fact that the accumulation of ions at the interface hinders the directional extraction of carriers by the CTL since  $R_{ct}$  reflects the carrier transfer ability.<sup>[39,40]</sup>

All the technical efforts and characterizations in this section are designed to ensure that when the bias voltage is applied, the additionally introduced ions will migrate rapidly. The redistributed ions control the location of voltage drop and dominate the wavelength-related photo-gain. In other words, it delivers spectrum richness. Meanwhile, the side effects introduced by the migration of intrinsic ions are relieved. That makes the repeated voltage stimulation possible.

### 2.3. The Construction and Performance Characterization of the Spectrometer

The final single-dot spectrometer is constructed on a chip based on the 5% LiCl-doped perovskite film, as shown in the schematic diagram in **Figure 4a**. A silver probe was adapted as the top electrode of the spectrometer. The active layer consists of an approximately 500 nm thick perovskite thin film sandwiched between the Spiro-OMeTAD layer and SnO<sub>2</sub> layer (Figure S9, Supporting Information). The thickness of the entire active area is approximately 700 nm with a working area footprint of only 440×440 μm<sup>2</sup>. To restore the unknown spectrum, the first step is to calibrate the light responsivity  $R$  of the spectrometer. Through the photocurrent when irradiated by monochromatic light, the mapping matrix  $R$  of the spectrometer can be calibrated. The typical current-voltage ( $I$ - $V$ ) curves at various wavelengths are displayed in Figure 4b. The responsivity under different pulse bias

modulation has also been calculated and exhibited in Figure 4c. The relationship between the external quantum efficiency and the bias is shown in Figure S10a (Supporting Information). It is clear that the photo-gain of the wavelength at approximately 630 nm increases with increasing bias, which corresponds to the main area with the voltage drop at the Spiro-OMeTAD/perovskite interface. As the bias reaches 0.5 V, the photo-gain at the wavelength of approximately 400 nm begins to increase since the main voltage drop area migrates to the ITO side, which is confirmed by the SIMS analysis. The  $I-t$  curves at zero bias were also measured (see Figure S10b, Supporting Information). In the absence of an external electric field, a rise time down to 800 ns is realized along with a decay time down to about 5  $\mu$ s. With the application of an external electric field, the rise and fall times of the spectrometer are gradually increasing since a longer ion balance time is required as the bias increases.<sup>[41,42]</sup> The relationship between the total response time and external bias is shown in Figure 4d (the detailed response curves are shown in Figure S10c and Figure S10d, Supporting Information). The sum of the rise and decay time of all modulation processes is used to define the total response speed. The response time under different external bias is measured and the total time which is expended for the achievement of different resolutions is calculated. The relationship between resolution and response time has also been evaluated (see Figure S11, Supporting Information). The limiting factors of response speed are mainly associated with two aspects. One is the balance time of ion redistribution and the other is the number of modulation times. When seeking higher resolution, higher bias

voltages are required. However, higher voltage means longer ion migration length and balance time. Hence, a balance between resolution and response time should be made. Of course, this is not like other spectrometers based on detector arrays that are fixed after manufacturing, this single-dot spectrometer can be “post-tuned” as needed.

To examine the reconstruction performance of the single-dot spectrometer for unknown spectra, we demonstrate the reconstruction of three different spectra with obvious characteristics, one of which is a white LED and the other two are a semiconductor laser and a halogen lamp (passed through band-pass filters with different bandwidths, see Figure S12, Supporting Information). The spectrum of the semiconductor laser is restored with 49 sampling points (see **Figure 5a**). We define the resolution as the minimum FWHM of the monochromatic light that the spectrometer can restore, which is consistent with the previous literature.<sup>[6]</sup> Normally, the FWHM of the restored spectrum is obviously wider than the measured spectrum. Such phenomenon is mainly affected by the number of sampling points. The resolution can be improved by increasing the number of tuning voltages or narrowing the operating range. As a result, a FWHM of 5.3 nm is obtained with 97 sampling points in an operating range of 200 nm. The spectra of other semiconductor lasers with various wavelengths have also been restored (see Figure 5b). As shown in Figure 5c (LED spectrum) and Figure 5d (halogen lamp), the reconstruction of wide-range spectra is also demonstrated. From these figures we can tell that the reconstructed and the measured spectral line present a good coincidence trend. The difference between the reconstructed

and the measured spectrum may come from the influence of measurement noise and the lack of resolution. There are mainly two aspects that can further improve the resolution: (1) improving the spectral feature richness of the response function. In other words, reducing the correlation between adjacent rows of the mapping matrix. (2) increasing the number of sampling points as well as the number of calibration data. For the first aspect, constructing a graded absorption layer may be a promising method. In this way, a small change in the tuning bias can reduce the row correlation of the mapping matrix. In addition, as Yuan introduced, this limiting factor might be alleviated if deep-learning method is used.<sup>[6]</sup> For the second aspect, the number of modulated voltages should be increased, and the light source used in the calibration process ought to be further optimized.<sup>[9]</sup> It should be noted that the monochromatic light employed in our calibration possess a FWHM of about 3.6 nm. That means even the number of voltage modulation can be increased, the calibration possess will still be restricted. Apart from that, the number of voltage modulation cannot also be increased unlimitedly. Due to the noise limitation, when the bias interval is sufficiently small, the change of the photo-current will become indistinguishable. Therefore, when we need a large number of voltage modulation, higher bias voltage (wider bias adjustment range) is inevitable. Unfortunately, high bias will potentially bring irreversible damage to the perovskite film. In the case of this experiment, a bias over 1 V will obviously does harm to the cycle stability. Therefore, a bias range of 0-0.7 V is chosen in this demonstration. Further improvement may rely on a new absorber design which can provide both the rich spectral



feature and high bias tolerance. At the current resolution, it takes about 850  $\mu\text{s}$  to reconstruct the laser spectrum, about 700  $\mu\text{s}$  to retrieve the halogen lamp spectrum, and approximately 197  $\mu\text{s}$  to restore the LED spectrum. In addition, for the reconstructed spectrum of the halogen lamp which passes through the narrowband filter, please refer to Figure S13 (Supporting Information). We further compare the characteristics of our single-dot spectrometer with some typical compact spectrometers in terms of the response speed, footprint and resolution (see Figure S14 and Table S1, supporting information). In addition to demonstrating the spectral reconstruction performance of the spectrometer, the other significant performance parameters are also investigated. Firstly, the influence of the random noise on reconstruction performance is simulated. It can be found that this spectrometer well resists the influence of noise (see Figure S1, Supporting Information), when the noise intensity is below 2%. The long-term operational stability of the spectrometer has also been explored. Under the irradiation of incident light (450 nm, 10.1  $\mu\text{W cm}^{-2}$ ), the photocurrent value did not alter significantly in the process of 1000 samples (see Figure S16, Supporting Information). The relationship between the photocurrent and light intensity is shown in Figure S17 (Supporting Information). This single-dot spectrometer exhibits a broad linear response range of 0.42  $\mu\text{W cm}^{-2}$  to 120  $\text{mW cm}^{-2}$ , and the measured LDR can reach 129 dB. When an external electric field is present, the photocurrent can still remain linear when the intensity is below 30  $\text{mW cm}^{-2}$ , and the corresponding calculated LDR is 46.9 dB. The above results represent the measurable range of light intensity for our spectrometer. The detectivity ( $D^*$ )

under various external bias voltages is measured and shown in Figure S18a and Figure S18b. It should be noted that at zero bias, device noise is mainly dominated by  $1/f$  noise (or flicker noise). When the external bias is applied, shot noise becomes the dominant factor (see Figure S19a and Figure S19b). As shown in Figure S19b, due to the appearance of shot noise, the noise current rises from several pA to several nA rapidly. As a result,  $D^*$  dropping from  $10^{11}$  Jones to  $10^9$  Jones is observed. When the bias increases, the photo-gain begins to take charge. However, photo-gain of the short wavelength mainly appears at high bias voltage. Therefore, even the  $D^*$  of around 700 nm wavelength reaches about  $6 \times 10^{10}$  Jones, it still maintains at about  $10^9$  Jones at wavelength around 400 nm. The signal-to-noise ratio (SNR) data also demonstrate the signal extraction ability of the spectrometer (see Figure S20, Supporting Information). To explore the influence of temperature on the device responsivity, various temperature and external bias are applied. Figure S21a, Figure S21b and Figure S21c correspond to the different incident light wavelengths which are 405 nm, 515 nm and 685 nm, respectively. In the temperature range of about 310 K - 230 K, the responsivity under different bias shows no obvious change. It means our device can work well under ambient temperature. The slight value change will not harm the device performance since a temperature-related correction matrix can be easily obtained. The high temperature restriction is mainly due to the organic hole transport layer (Spiro-OMeTAD).<sup>[43]</sup> The low temperature restriction is mainly attributed to the freezing of ion migration. Not surprisingly, for all the wavelengths, there exist trip points around the temperature of 210 K

(slightly affected by the external bias). It happens to be the temperature threshold of ion migration (see Figure 2a). When the temperature is lower than the threshold, the ion redistribution induced by the external bias will disappear.<sup>[44]</sup> It should be noted that the photo-gain is usually believed to be derived from the unbalanced carriers. When the external bias is applied, the ion redistribution occurs. Owing to the lowest activation energy, it is mainly be the halogen ions. Therefore, at the redistribution area, a large number of halogen vacancies will exist. Such vacancy can serve as hole (minority carrier) trapping center which prolongs the life time of minority carriers and provides the photo-gain. However, when the ion migration is frozen, the origin of the photo-gain is restricted, which results in the rapid decrease of responsivity.

This micron-level device area and fast response speed provides the basis for future compact on-chip integrated spectral imaging components. Here, we propose an on-chip integrated spectral imaging system, as illustrated in Figure 5e-g. When the imaging system receives the composite light reflected by the object, a single pixel can be utilized to determine the detailed colour information. Through data measurement and data filtering, we can attain a spectral data cube. Finally, the image information of the arch can be reconstructed with an ultrahigh colour resolution and a short shutter time, which is a major improvement for both traditional photography systems and advanced hyperspectral sensing. The very large amount of spectral data provided inside one image also promotes future

machine vision and big data analysis applications (more details please see experimental section, Supporting Information).<sup>[45]</sup>

### 3. Conclusion

Here, we report a single-dot spectrometer based on an in situ modulated perovskite photodetector. The LiCl additive suppressed and replaced the original ion migration and created a perovskite detector with a tunable photo-gain through controllable ion redistribution. Without any optical or mechanical component, such a single-dot spectrometer achieves spectral recognition with a resolution of about 5 nm in the micron-level active area. Our demonstration leads to a new direction of perovskite in situ modulation for the development of new functional devices.

### Supporting Information

Supporting Information is available from the Wiley Online Library or from the author.

### Acknowledgements

**Funding:** This work was supported by the National Natural Science Foundation of China (52025028, 51772197, 51872191, 52072254 and 52002258), 1000 Youth Talents Plan, the

Natural Science Foundation of Jiangsu Province (BK20200877, BK20210728), and Funded by the Priority Academic Program Development (PAPD) of Jiangsu Higher Education Institutions.

**Competing Interests:** All other authors declare they have no competing interests.

Received: ((will be filled in by the editorial staff))

Revised: ((will be filled in by the editorial staff))

Published online: ((will be filled in by the editorial staff))

## References

- [1] M. Manley, *Chem. Soc. Rev.* **2014**, *43*, 8200.
- [2] M. R. Torr, D. G. Torr, *Science*, **1984**, *225*, 169.
- [3] C. P. Bacon, Y. Mattley, R. DeFrece, *Rev. Sci. Instrum.* **2004**, *75*, 1460.

This article is protected by copyright. All rights reserved.

- [4] N. Savage, *Nat. Photonics*. **2009**, *3*, 601.
- [5] B. Redding, S. F. Liew, R. Sarma, H. Cao, *Nat. Photonics*. **2013**, *7*, 746.
- [6] S. Yuan, D. Naveh, K. Watanabe, T. Taniguchi, F. Xia, *Nat. Photonics*. **2021**, *15*, 601.
- [7] J. Bao, M. G. Bawendi, *Nature*. **2015**, *523*, 67.
- [8] H. Sun, W. Tian, X. Wang, K. Deng, J. Xiong, L. Li, *Adv. Mater.* **2020**, *32*, 1908108.
- [9] Z. Yang, T. Albrow-Owen, H. Cui, J. Alexander-Webber, F. Gu, X. Wang, T. C. Wu, M. Zhuge, C. Williams, P. Wang, A. V. Zayats, W. Cai, L. Dai, S. Hofmann, M. Overend, L. Tong, Q. Yang, Z. Sun, T. Hasan, *Science*. **2019**, *1020*, 1017.
- [10] A. Li, Y. Fainman, *Nat. Commun.* **2021**, *12*, 2704.
- [11] D. M. Kita, B. Miranda, D. Favela, D. Bono, J. Michon, H. Lin, T. Gu, J. Hu, *Nat. Commun.* **2018**, *9*, 4405.
- [12] R. Cheng, C. L. Zou, X. Guo, S. Wang, X. Han, H. X. Tang, *Nat. Commun.* **2019**, *10*, 4104.
- [13] J. Meng, J. J. Cadusch, K. B. Crozier, *Nano Lett.* **2020**, *20*, 320.
- [14] S. N. Zheng, J. Zou, H. Cai, J. F. Song, L. K. Chin, P. Y. Liu, Z. P. Lin, D. L. Kwong, A. Q. Liu, *Nat. Commun.* **2019**, *10*, 2349.

- [15] Z. Yang, T. Albrow-Owen, W. Cai, T. Hasan, *Science*. **2021**, *371*, eabe0722.
- [16] R. F. Wolffenbuttel, *IEEE Trans. Instrum. Meas.* **2004**, *53*, 197.
- [17] A. V. Velasco, P. Cheben, P. J. Bock, A. Del  ge, J. H. Schmid, J. Lapointe, S. Janz, M. L. Calvo, D.-X. Xu, M. Florja  czyk, M. Vachon, *Opt. Lett.* **2013**, *38*, 706.
- [18] Y. Fang, Q. Dong, Y. Shao, Y. Yuan, J. Huang, *Nat. Photonics*. **2015**, *9*, 679.
- [19] L. Li, Y. Deng, C. Bao, Y. Fang, H. Wei, S. Tang, F. Zhang, J. Huang, *Adv. Opt. Mater.* **2017**, *5*, 1700672.
- [20] W. Qarony, M. Kozawa, H. A. Khan, M. I. Hossain, A. Salleo, Y. H. Tsang, J. Y. Hardeberg, H. Fujiwara, D. Knipp, *Adv. Mater. Interfaces*. **2020**, *7*, 2000459.
- [21] N. Ganesh, R. Shivanna, R. H. Friend, K. S. Narayan, *Nano Lett.* **2019**, *19*, 6577.
- [22] Z. A. VanOrman, L. Nienhaus, *InfoMat*. **2021**, *3*, 962.
- [23] Q. Lin, A. Armin, P. L. Burn, P. Meredith, *Nat. Photonics*. **2015**, *9*, 687.
- [24] Y. An, A. Shang, G. Cao, S. Wu, D. Ma, X. Li, *Sol. RRL*. **2018**, *2*, 1800126.
- [25] H. Sun, K. Deng, J. Xiong, L. Li, *Adv. Energy Mater.* **2020**, *10*, 1903347.
- [26] P. Cui, D. Wei, J. Ji, H. Huang, E. Jia, S. Dou, T. Wang, W. Wang, M. Li, *Nat. Energy*. **2019**, *4*, 150.

- [27] B. Huang, J. Liu, Z. Han, Y. Gu, D. Yu, X. Xu, Y. Zou, *ACS Appl. Mater. Interfaces*. **2020**, 12, 48765
- [28] W. Tian, L. Min, F. Cao, L. Li, *Adv. Mater.* **2020**, 32, 1906974.
- [29] V. Nandal, P. R. Nair, *ACS Nano*. **2017**, 11, 11505.
- [30] J. Huang, Y. Yuan, Y. Shao, Y. Yan, *Nat. Rev. Mater.* **2017**, 2, 17042
- [31] L. Qiao, W. H. Fang, R. Long, O. V. Prezhdo, *ACS Energy Lett.* **2020**, 5, 3813.
- [32] F. Giordano, A. Abate, J. P. Correa Baena, M. Saliba, T. Matsui, S. H. Im, S. M. Zakeeruddin, M. K. Nazeeruddin, A. Hagfeldt, M. Graetzel, *Nat. Commun.* **2016**, 7, 10379.
- [33] J. Cao, S. X. Tao, P. A. Bobbert, C. P. Wong, N. Zhao, *Adv. Mater.* **2018**, 30, 1707350.
- [34] B. Yang, C. C. Brown, J. Huang, L. Collins, X. Sang, R. R. Unocic, S. Jesse, S. V. Kalinin, A. Belianinov, J. Jakowski, D. B. Geohegan, B. G. Sumpter, K. Xiao, O. S. Ovchinnikova, *Adv. Funct. Mater.* **2017**, 27, 1700749.
- [35] M. Wang, F. Cao, K. Deng, L. Li, *Nano Energy*. **2019**, 63, 103867.
- [36] C. J. Tong, L. Li, L. M. Liu, O. V. Prezhdo, *ACS Energy Lett.* **2018**, 3, 1868.
- [37] X. Jiang, J. Hoffman, C. C. Stoumpos, M. G. Kanatzidis, E. Harel, *ACS Energy Lett.* **2019**, 4, 1741.



- [38] P. Calado, P. R. F. Barnes, *Nat. Energy*. **2021**, *6*, 589.
- [39] L. Contreras-Bernal, S. Ramos-Terrón, A. Riquelme, P. P. Boix, J. Idígoras, I. Mora-Seró, J. A. Anta, *J. Mater. Chem. A*. **2019**, *7*, 12191.
- [40] A. R. Pascoe, N. W. Duffy, A. D. Scully, F. Huang, Y. B. Cheng, *J. Phys. Chem. C*. **2015**, *119*, 4444.
- [41] J. M. Ball, A. Petrozza, *Nat. Energy*. **2016**, *1*, 16149.
- [42] L. Li, F. Wang, X. Wu, H. Yu, S. Zhou, N. Zhao, *J. Phys. Chem. C*. **2016**, *120*, 2536.
- [43] N. J. Jeon, H. Na, E. H. Jung, T. Y. Yang, Y. G. Lee, G. Kim, H. W. Shin, S. Il Seok, J. Lee, J. Seo, *Nat. Energy*. **2018**, *3*, 682.
- [44] M. Chen, X. Shan, T. Geske, J. Li, Z. Yu, *ACS Nano*. **2017**, *11*, 6312.
- [45] P. Wu, T. He, H. Zhu, Y. Wang, Q. Li, Z. Wang, X. Fu, F. Wang, P. Wang, C. Shan, Z. Fan, L. Liao, P. Zhou, W. Hu, *InfoMat*. **2022**, *4*, e12275.

## Figures and Captions

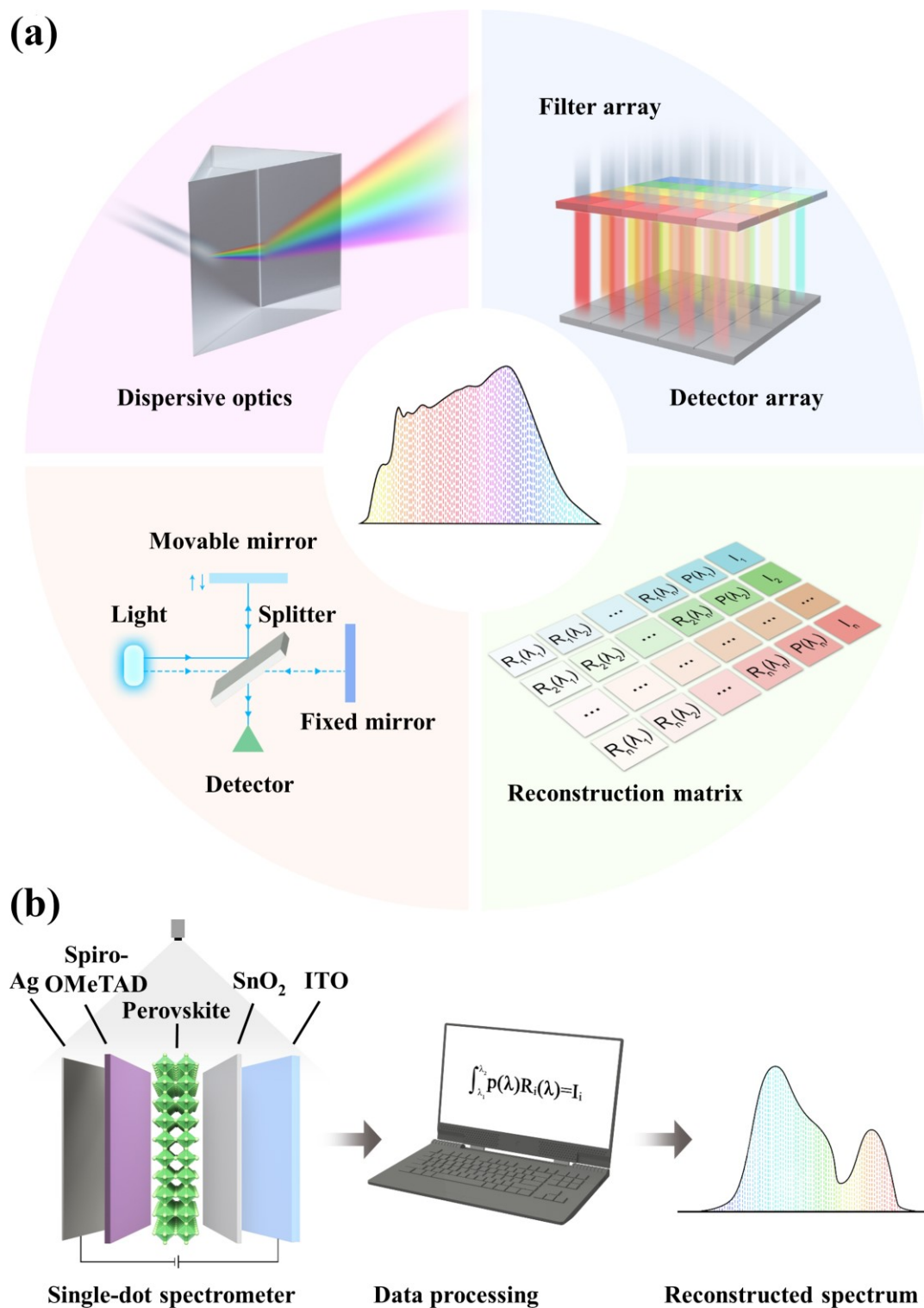


**Figure 1.** Classification of the mechanism of the spectrometer. (a) Mechanisms from previous literature and (b) schematic showing the mechanism of our single-dot perovskite spectrometer.

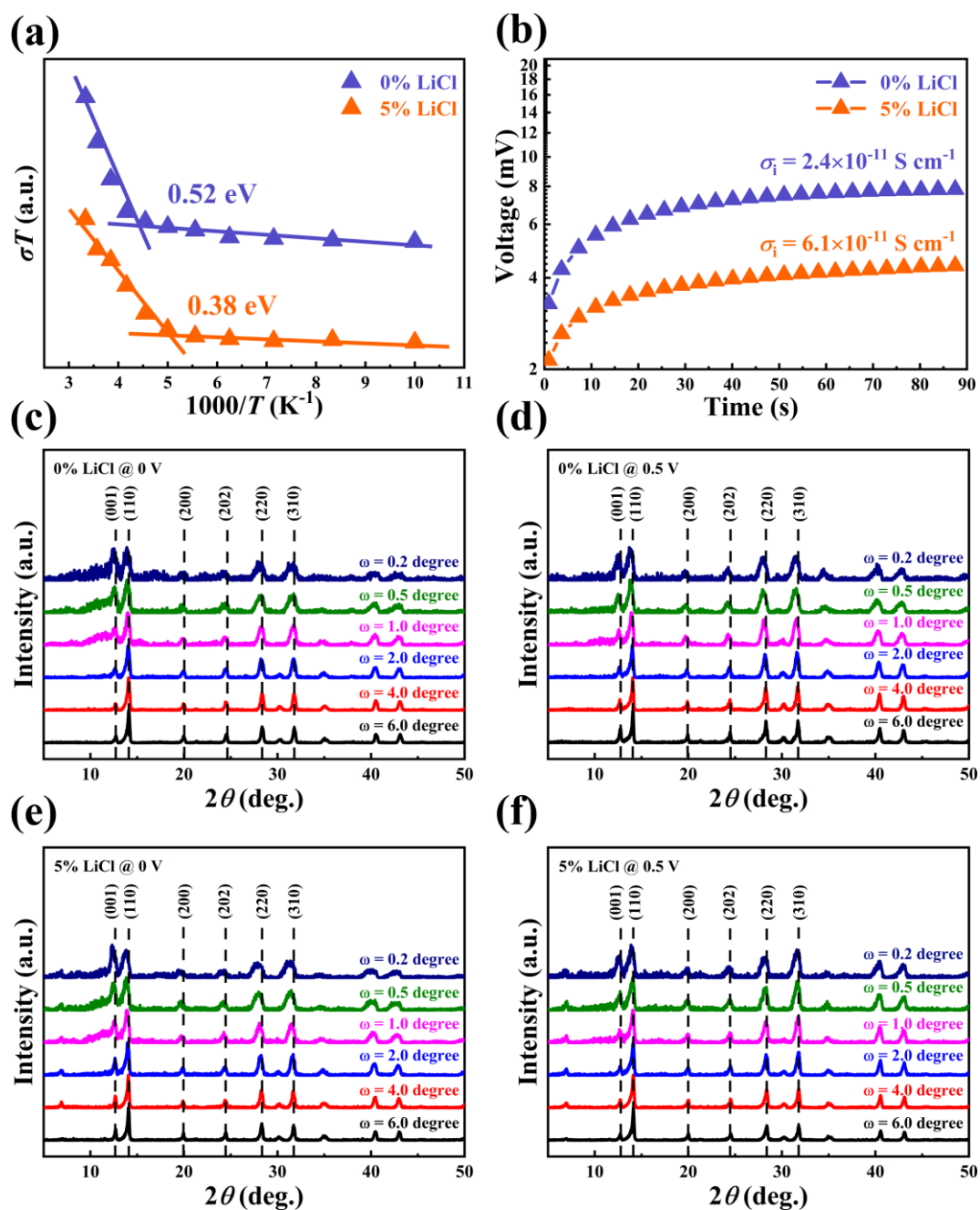
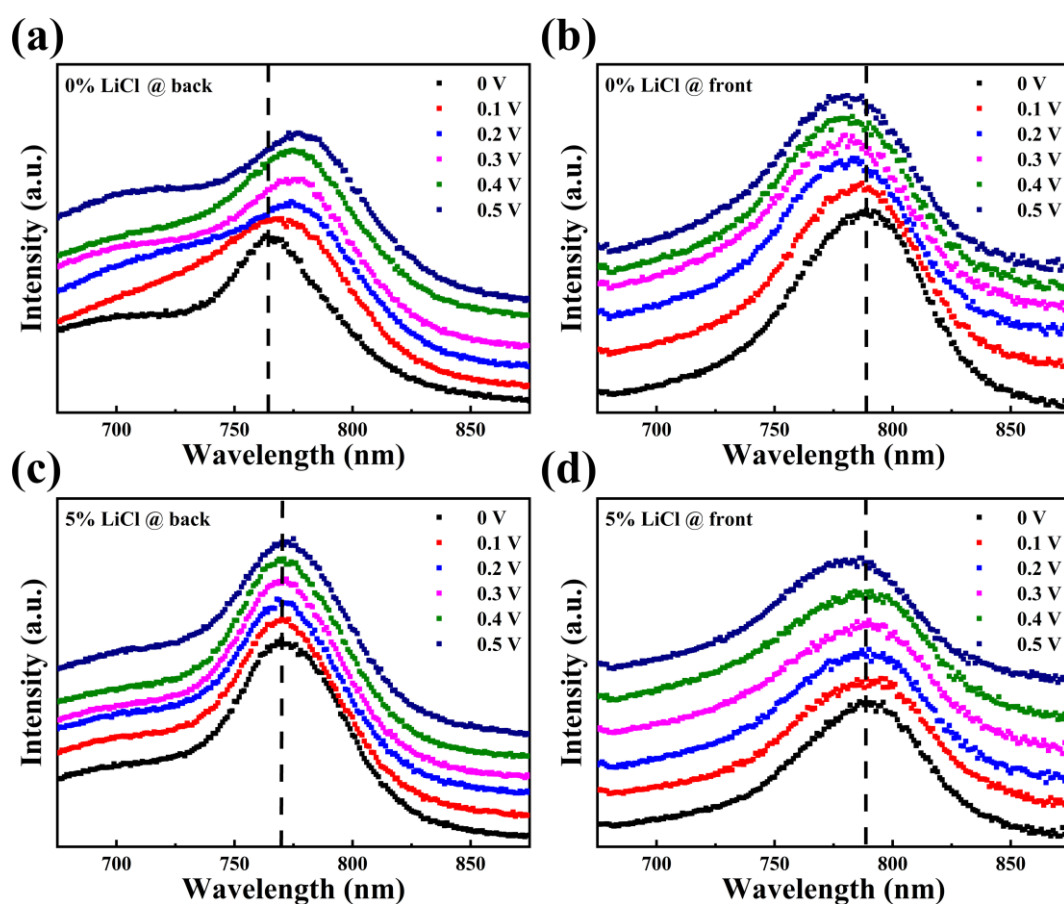


**Figure 2.** Characterization of ion redistribution in the perovskite. (a) Temperature-dependent conductivity of the perovskite with/without doping. (b) Polarization curves in the

Au/perovskite/Au device measured by applying a constant current of 0.5 nA. GIXRD patterns of the (c) control sample and (d) 5% LiCl-doped sample without polarization under an external bias. GIXRD patterns of the (e) control sample and (f) 5% LiCl-doped sample just after polarizing under a 0.5 V external bias.



This article is protected by copyright. All rights reserved.

**Figure 3.** PL spectra of devices with semi-transparent electrodes. (a) Control sample after polarizing at different biases and heading from the ITO side and (b) Spiro-OMeTAD side towards the excitation source. (c) 5% LiCl-doped sample when heading from the ITO side and (d) Spiro-OMeTAD side towards the excitation source.

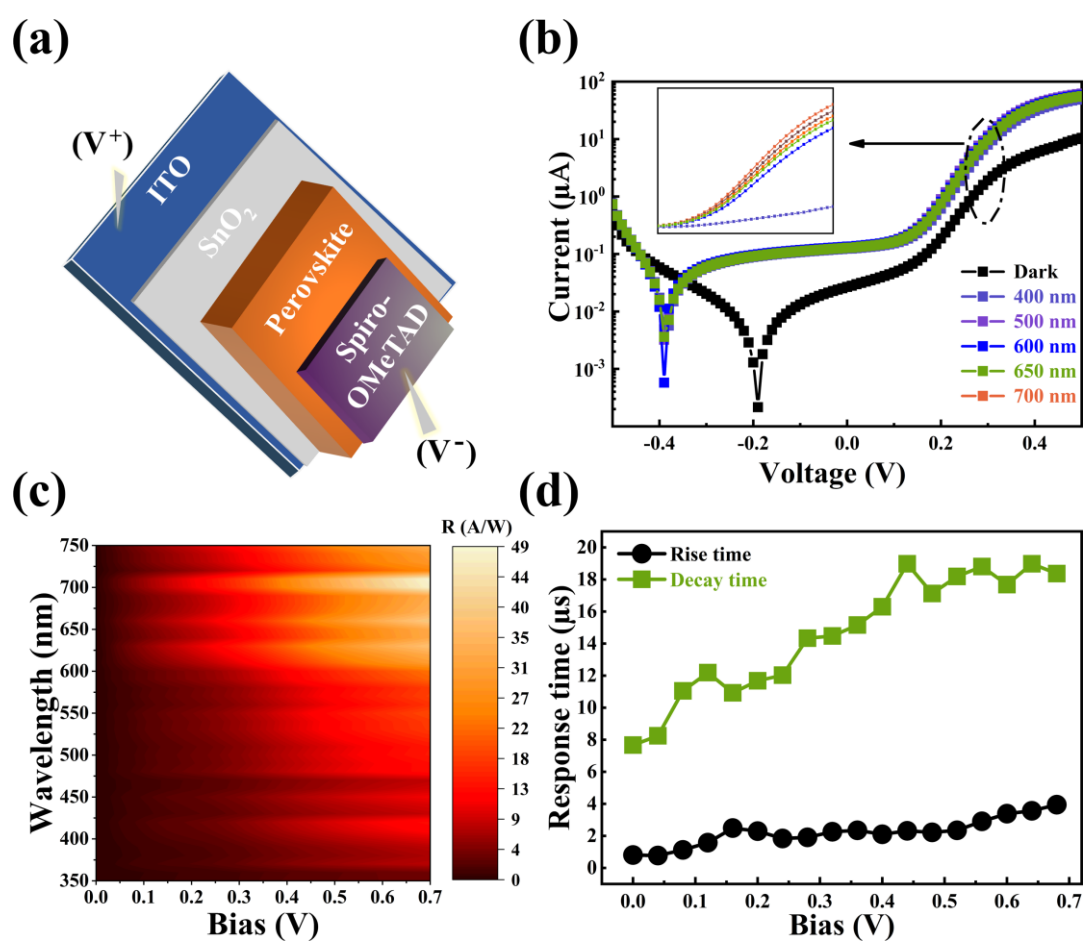
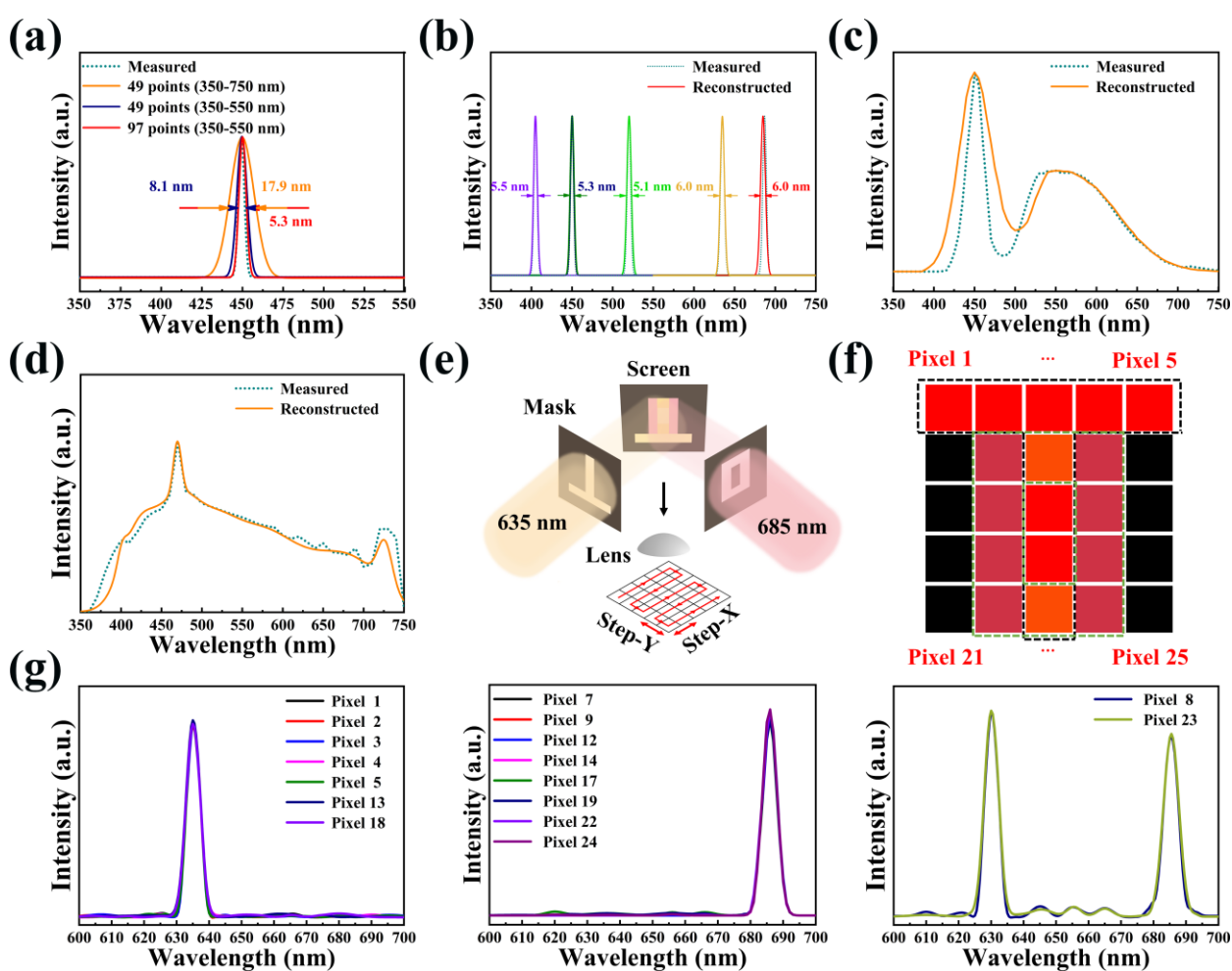


**Figure 4.** Performance evaluation of the single-dot spectrometer. (a) Schematic showing the structure of the single-dot spectrometer. (b)  $I$ - $V$  curves of the spectrometer when irradiated

by monochromatic light at various wavelengths. (c) Photoresponsivity of the spectrometer as a function of the applied bias and wavelength. (d) Relationship between the response time and external bias voltage.



This article is protected by copyright. All rights reserved.

**Figure 5.** Spectrum reconstruction of the single-dot spectrometer. (a) The comparison of spectrum reconstruction with different sampling points under illumination of 450 nm laser. The measured and reconstructed spectrum under the illumination of (b) semiconductor lasers with different wavelengths, (c) LED and (d) halogen lamp. (e) Measurement set-up. The imaging target is a mix of a number “0” and a letter “T”, where the “T” consists of 635 nm monochromatic light and the “0” consists of 685 nm monochromatic light. (f) Arrangement of these 25 pixels. (g) The spectra of each pixel reconstructed by the spectrometer.

A single-dot perovskite spectrometer is demonstrated, which firstly breaks the long-standing restriction of footprint-resolution. The control of ion migration in perovskite is the key of spectrum richness and cyclic stability. Without any optical and mechanical structure, the spectrum can be recognized by a single detector through the bias stimulated photo-gain modulation.



